Hindawi
Advances in Materials Science and Engineering
Volume 2022, Article ID 8771674, 12 pages
https://doi.org/10.1155/2022/8771674

Research Article

Experimental Study on Fracture Properties of Hydraulic Concrete with Different Crack-Depth Ratios Based on Acoustic Emission and DIC Techniques

Yingjie Ning[1], **Linjie Ye**[2], **Lihui Bai**[1], **Chunhui Xie**[2] and **Huiying Xu**[3]

[1]*Zhejiang Communications Construction Group Co. Ltd, Hangzhou 310000, Zhejiang, China*
[2]*Zhejiang Communications Construction New Material Co. Ltd, Hangzhou 310000, Zhejiang, China*
[3]*College of Hydraulic Science and Engineering, Yangzhou University, Yangzhou 225000, Jiangsu, China*

Correspondence should be addressed to Yingjie Ning; ningyingjie1972@163.com

Received 21 August 2022; Revised 20 October 2022; Accepted 9 November 2022; Published 3 December 2022

Academic Editor: Yuri Ribakov

In order to study the fracture behavior of hydraulic concrete, wedge splitting tests are performed on notched cubic concrete specimens with different crack-depth ratios (0.3, 0.4, and 0.5). Meanwhile, acoustic emission and the digital image correlation method were used to monitor the crack propagation. Test results show that the initiation toughness of the hydraulic concrete specimen is independent of the crack-depth ratio. As the crack-depth ratio increases, the fracture toughness, the fracture energy, and the critical crack length decrease. The AE cumulative counts and hits can reflect not only the four-stages fracture process of hydraulic concrete but also the boundary effect of hydraulic concrete. The acoustic emission b value can reflect the two stages of postpeak damage of the hydraulic concrete. The length of fictitious crack, the propagation velocity of macrocrack and effective crack length decrease with the increase of the initial notch depth ratio. The effective crack length increases with the increase in the maximum aggregate size, and the growth time increases with the maximum aggregate size and an effective height of the specimen.

1. Introduction

Since fracture mechanics is first applied to concrete by Kaplan [1] in 1961, Hoover, and Bazant have conducted extensive studies on the effect of initial crack-depth ratio on the fracture properties of hydraulic concrete [2–5]. Xu et al. [6] conducted three-point bending experiments on 60 groups of notched concrete beams of different sizes to determine the influence of boundary effect on fracture energy. Hu et al. [7] found that the initial crack-depth ratio had little effect on the initiation fracture toughness but some effect on the unstable fracture toughness by wedge splitting test and extended finite element simulation. When the crack-depth ratio was less than 0.4, the fracture toughness increased with the increasing of initial crack-depth ratio for axial tension, bending, and splitting tension tests [8]. The results indicate that the initiation fracture toughness and the unstable fracture toughness are dependent on the crack-depth ratio. But other fracture parameters need further study. The effect of the crack-depth ratio on the fracture toughness of concrete is different due to the raw materials and test conditions [9], in which the maximum particle size of the aggregate plays a key role in crack extension [10–12]. Hydraulic concrete uses three to four grades aggregates, and the content of the cement paste and aggregate differs from ordinary concrete. Stronger aggregate interlocking effects are more pronounced in hydraulic concrete [13, 14]. Xu et al. [15] analyzed the failure mode of bulk concrete under three-point bending loading and obtained that the heterogeneity of concrete was the main reason affecting the crack propagation path. In previous studies, due to the limitations of test conditions, specimen size, and equipment, small wet sieved specimens with particle sizes smaller than 40 mm were usually used instead of hydraulic concrete to study its mechanical properties. The test results did not truly reflect the mechanical properties of hydraulic concrete [16–18].

Table 1: The mix proportion of hydraulic concrete kg·m^{-3}.

Mix	Water	Cement	Sand	Fly ash	Aggregate				Water reducing agent
					Small	Medium	Large	XLA	
MP1	138.0	210.0	711.0	90.0	375.0	375.0	500.0		6.3
MP2	115.0	150.8	591.0	81.2	400.0	320.0	400.0	180.0	2.7

Therefore, it is necessary to analyze the fracture behavior of full-graded hydraulic concrete.

As a nondestructive testing method, the acoustic emission technique is widely used in concrete fracture research. Panjsetooni et al. [19] calculated the static pressure ratio and load ratio by the number of AE events, and the variation trend of these two values can predict the remaining service life of concrete. Chen et al. [20] found that the acoustic emission b-value can reflect three stages of concrete crack expansion under different loading rates; Abouhussein and Hassan [21] analyzed acoustic emission b-value and amplitude, which well assessed the damage degree of self-compacting rubber concrete. The digital image correlation (DIC) method can monitor the deformation evolution process and determine the information of crack location, morphology, and expansion direction, and it has been widely used in engineering and academic areas in recent years. Dai et al. [22] used the DIC technique to determine the crack and the FPZ length during crack propagation. Pereira et al. [23] applied DIC to study crack development in concrete beams. Previous work mainly used DIC methods for strain clouds and crack opening displacements and mainly focused on the study of fracture patterns in small-size concrete, while there were fewer studies on crack expansion patterns in large-size fully graded concrete during the whole damage process.

To investigate the fracture behavior of dam concrete with different crack-depth ratios, Wedge splitting tests are performed on notched cubic hydraulic concrete specimens with three different crack-depth ratios (0.3, 0.4, and 0.5). The acoustic emission technique and digital image correlation method are used to monitor the crack propagation.

2. Materials and Test Methods

2.1. Materials. The objects of this paper are three-graded and full-graded dam concrete. The raw materials used for pouring concrete are tap water, cement with P.O 42.5, secondary fly ash used as a mineral admixture to reduce the early heat of hydration of the hydraulic concrete, well-graded river sand as fine aggregate, and granite gravel with a maximum particle size of 80 mm or 120 mm as a coarse aggregate. In addition, a polycarboxylic acid superplasticizer was added to improve the fluidity of the concrete mixture. Two kinds of hydraulic concrete of mix proportions are used, as shown in Table 1. The specimen with a side length of 300 mm noted as MP I, and the specimen with side length of 450 mm noted as proportion II.

The concrete mixture was poured into the wood formworks, which was disassembled 24 hours later. The formed concrete specimens were cured for 27 days in the curing room. The specimen was taken out, and an initial crack was prefabricated by using a cutting machine. The crack width was 2 mm, and the crack (a) to height (H) ratios α were set as 0.3, 0.4, or 0.5. Concrete specimens with different crack-depth ratios are denoted by symbols of "WS," "side length," and "crack-depth ratio." For example, WS 300-0.3 denotes a cubic specimen with a side length of 300 mm and a crack-depth ratio of 0.3.

To test the tensile strength of concrete specimens, cylindrical core samples with a height of 285 mm and a diameter of 142.5 mm were drilled from the cubic specimens. The axial tensile strengths of concrete specimens MP1 and MP2 are 2.30 MPa and 1.05 MPa, respectively.

2.2. Wedge Splitting Test. The wedge splitting test was carried out by using the hydraulic closed-loop microcomputer servo material testing machine MTS322, as shown in Figure 1. The loading process was controlled by crack mouth opening displacement (CMOD), and the loading rate was 0.001 mm/s. The clip extensometer was installed between the steel edges on both sides of the initial crack notch at the top of the specimen to measure and control the CMOD value. To eliminate the bending moment and vertical load by specimen weight, two steel bars are used as supports at the quadrant of the specimen. The wedge steel plate converts the vertical load P_v into the horizontal load P imposed on the specimen through the roller on the I-steel. The relationship between the horizontal load and the vertical load can be expressed as follows:

$$P = \frac{P_v}{2\mathrm{tg}\theta}, \tag{1}$$

where θ represents the wedge angle, here is 15°.

2.3. Acoustic Emission Test. The acoustic emission parameters of all specimens were collected by the Sensor Highway II 8-channel acquisition system, produced by the American Physical Acoustics Company. Through a pretest and field noise level evaluation, the threshold value and pregain are set as 35 dB, and the filtering frequency is 1–60 kHz. Four acoustic emission probes are installed on the front and back of the specimen, and it is ensured that the probes are not on the same horizontal line.

2.4. DIC Test Method. The digital image correlation method can accurately determine the crack initiation and propagation processes at any point in the test zone. A high-speed camera is used to take a series of grayscale images on the surface of the specimen with speckle (as shown in Figure 2), and the displacement of speckle during the loading process is calculated by digital image correlation method. So the surface displacement field of the specimen can be obtained. The calculation process in detail as follows: The test area is divided into 70 horizontal

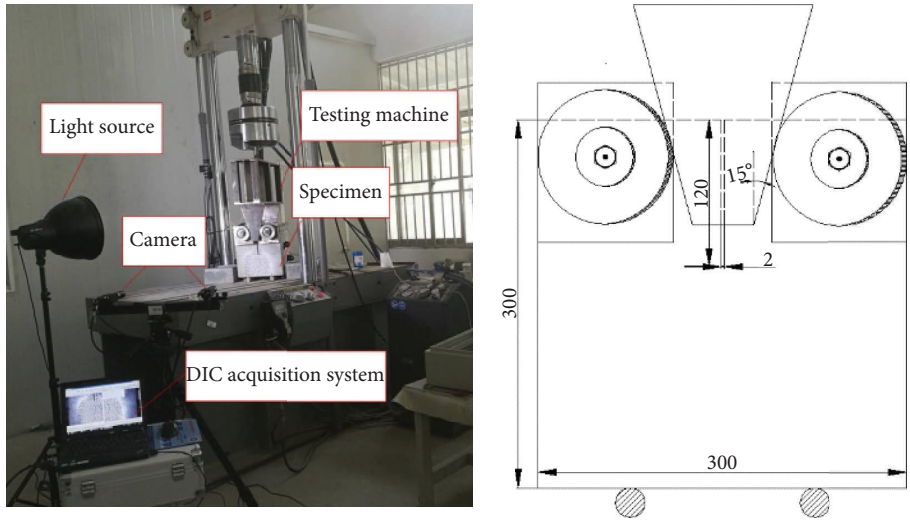

Figure 1: Wedge splitting tensile test device. (a) Physical drawing. (b) Schematic drawing.

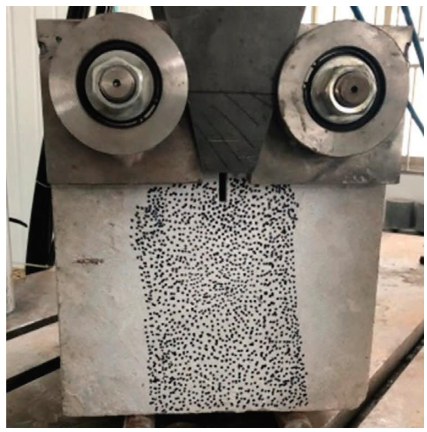

Figure 2: Specimen surface with speckle.

areas and 248 vertical areas, generating 17,043 nodes in total, as shown in Figure 3(a). The crack opening displacement (COD) of each node along the crack propagation direction was calculated. For example, to calculate the opening displacement at the crack tip of the specimen, it is necessary to calculate the change of node displacement. Figure 3(b) shows the horizontal displacement distribution of crack tip when WS300-0.3 specimen was loaded to 5% P_{max} after peak. It can be seen from Figure 3(b), the value of displacement on the left side of crack is negative, and that on the right side is positive. The displacement change suddenly at some certain location, where the fracture process zone occurs. The width of the fracture process zone equals to the distance between two points (points A and B) where displacement changes suddenly. And the crack opening displacement between two points A and B is 1.3 mm.

3. Test Results and Analysis

3.1. Fracture Properties. Figure 4 shows the P-CMOD curves of specimens with different crack-depth ratios. It can be seen that, with the increase of the crack-depth ratio, the slope of the prepeak branch gradually decreases, the slope of the postpeak branch gradually slows down, and the peak load gradually decreases. It indicates that with the increase of the crack-depth ratio, the smaller the energy is required for the specimen for fracture. The postpeak behavior of specimen MP2 with maximum aggregate size of 120 mm is more stable.

Double-k fracture theory can be used to determine the fracture process of concrete specimens [24]. The initial fracture toughness and unstable fracture toughness can be calculated as the following formulas:

$$K_{\mathrm{IC}}^{\mathrm{S}} = \frac{P_{\max} \times 10^{-3}}{th^{1/2}} f(\alpha),$$
$$K_{\mathrm{IC}}^{\mathrm{Q}} = \frac{P_{\mathrm{Q}} \times 10^{-3}}{th^{1/2}} f(\alpha). \tag{2}$$

In which

$$f(\alpha) = \frac{3.675[1 - 0.12(\alpha - 0.45)]}{(1-\alpha)^{3/2}},$$
$$a_c = (h + h_0)\left[1 - \left(\frac{13.18}{\mathrm{CMOD}_c \cdot E \cdot t / P_{\max} + 9.16}\right)^{1/2}\right] - h_0,$$
$$E = \frac{1}{tc_i}\left[13.18\left(1 - \frac{a_0 + h_0}{h + h_0}\right)^{-2} - 9.16\right],$$
$$P_{\max} = \frac{P_{v\max}}{2\mathrm{tg}15^{\circ}},$$
$$P_{\mathrm{Q}} = \frac{P_{v\mathrm{Q}}}{2\mathrm{tg}15^{\circ}}, \tag{3}$$

where K_{IC}^{S} is unstable fracture toughness (MPa·m$^{1/2}$), K_{IC}^{Q} is initial fracture toughness (MPa·m$^{1/2}$), t is the thickness of

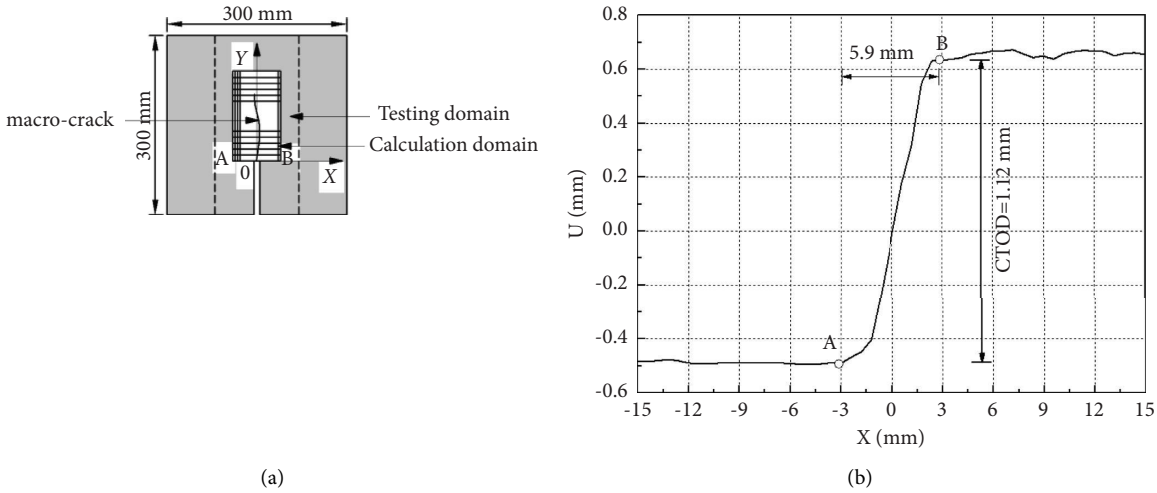

Figure 3: Diagram on the calculation method of crack opening displacement. (a) Testing zone. (b) Displacement along X direction.

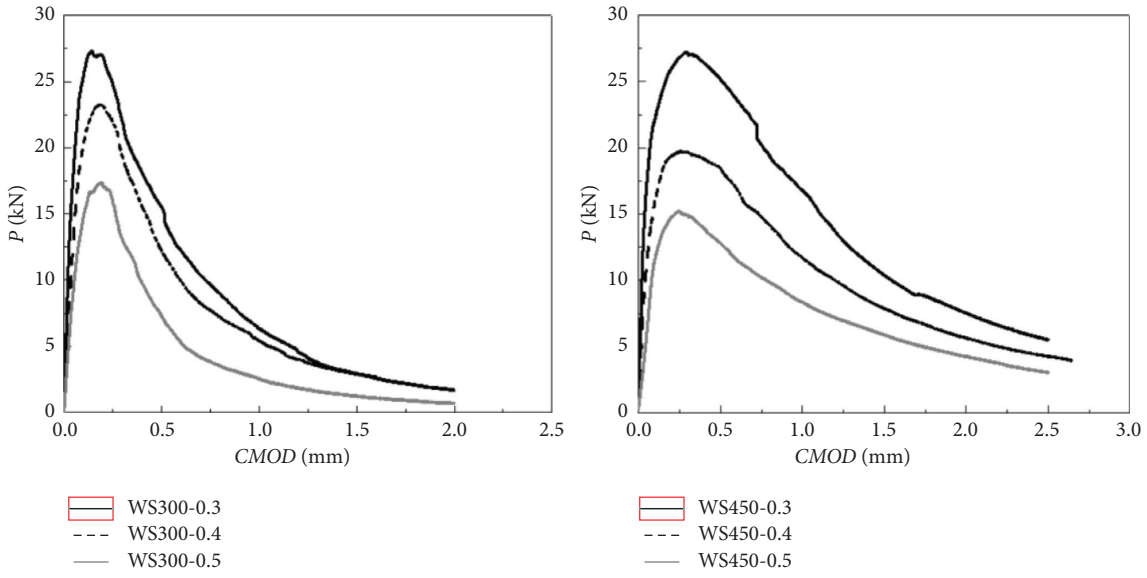

Figure 4: P-CMOD curves of hydraulic concrete specimens.

specimen (m), h is the height of the specimen (m), a_c is the effective crack length (m), P_{max} is the maximum load (kN), and P_Q is the initial crack load (kN), which is corresponding to the load when the P-CMOD curve begins to turn from linear to nonlinear. The crack initial load can be determined as follows, make a tangent line from the start point of P-CMOD curve, which is probably coincide with the P-CMOD curve as it is linear at the beginning. The load corresponds to the point where the tangent line begins to departure from the P-CMOD curve, can be regard as the crack initial load. P_v is vertical load (kN). h_0 is the thickness (m) of the thin of steel plate. α is the ratio of crack depth to height of specimen. The effective crack length a_c is selected when calculating the unstable fracture toughness, and the initial crack height a_0 is selected when calculating the initial fracture toughness. E is the elastic modulus (GPa) and $CMOD_c$ is the critical value of crack opening displacement and c_i is the initial compliance (μm/kN), which equals to the ratio of CMOD to P.

The fracture toughness of concrete can be calculated according to the P-CMOD curve as shown in Table 2. It can be seen that the initial fracture toughness of cubic specimens has changes little with the increase of the crack-depth ratio, but the unstable fracture toughness decreases with the increase of the crack-depth ratio. The results show that the initial fracture toughness of cubic specimens with different side lengths is basically unchanged with the change of the crack depth ratio, which can be regarded as a constant. So it can be used as the basis for judging the initial fracture of concrete specimens. The fracture toughness decreases with the increase of the crack-depth ratio, probably because the specimen is less constrained by the back boundary with the increase of the crack-depth ratio.

Table 2: The fracture parameters of hydraulic concrete.

Specimen	P_{max} (kN)	K_{IC}^{Q} (MPa·m$^{1/2}$)	K_{IC}^{S} (MPa·m$^{1/2}$)	G_F (N·m^{-1})	a_c (mm)	Δa_c (mm)
WS300-0.3	27.31	0.74	2.04	350.76	167.06	77.06
WS300-0.4	23.27	0.78	1.95	347.73	176.83	56.83
WS300-0.5	17.38	0.77	1.89	241.50	197.36	47.36
WS450-0.3	27.21	0.40	1.05	354.58	243.47	108.47
WS450-0.4	19.77	0.38	0.98	309.40	276.29	96.92
WS450-0.5	15.23	0.39	0.82	264.67	285.46	60.46

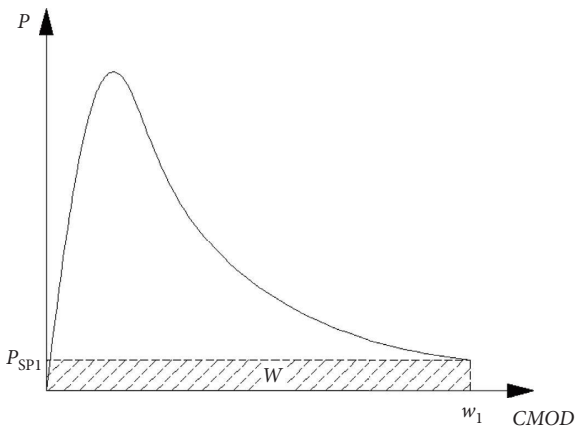

Figure 5: The determination method of tail fracture energy.

The effective crack length of hydraulic concrete increases with the increase in crack-depth ratio, and the critical crack propagation Δa_c ($\Delta a_c = a_c - a_0$) decreases with the increase of the crack-depth ratio. The critical expansion can effectively characterize the fracture toughness. The larger the value of critical crack expansion is, the more fully the crack expansion is and the better the toughness of the specimen is. Therefore, the smaller the crack-depth ratio is, the better the toughness of the fracture is. In addition, fracture energy is a commonly used indicator to reflect the toughness of materials. Fracture energy refers to the energy consumed per unit area of fracture expansion, which can be calculated by the following formula:

$$G_F = \frac{W}{A_{tig}} = \frac{W}{th}, \tag{4}$$

in which G_F is the fracture energy (N·m^{-1}), W is the area enclosed by P-CMOD curve and abscissa (N·mm), A_{tig} is the area of ruptured ligament (mm^2), t is the thickness of the specimen (mm), and H is the height of the specimen (mm).

During the test, it was difficult to load until the specimen fractured completely. Therefore, it is necessary to modify the test tail. According to the method proposed by Ulfkjer et al. [25], the area W enclosed by the load PSP1 at the end of the test and the corresponding crack opening displacement W_1 on the P-CMOD curve and the abscissa is divided by the fracture area as shown in Figure 5, denoted as tail fracture energy. The sum of the tail fracture energy and formula (4) calculated from the test curve is the total fracture energy.

The fracture energy data calculated by using the modified method is shown in Table 2. It can be seen that the fracture energy of hydraulic concrete specimens decreases with the increase of the crack-depth ratio, regardless of the specimen side length. On the one hand, the smaller the crack-depth ratio is, the greater the rupture ligament area of the concrete specimen is. And influenced by the large sizes of aggregate, cracks are less likely to run through the strong aggregate. In most cases crack occurs at the interface between aggregate and mortar instead of aggregate. So the required energy to fracture the concrete increases with the increasing size of the aggregate. On the other hand, there is a stable fracture zone at the crack tip. In this area, the fracture energy is a constant, which is called local fracture energy. When the crack extends to boundary, the fracture energy decreases. Therefore, when the crack-depth ratio of the specimen increases; that is, when the effective height decreases, the more obvious the boundary effect is, the smaller the fracture energy is.

3.2. Acoustic Emission Characteristics

3.2.1. AE Events. The cumulative AE events can be used for AE activity evaluation, which can reflect the change and development process of cracks in concrete specimens. Figure 6 shows the variations of load and cumulative AE events. It can be found that the AE events curve can be divided into four stages, which reflect the failure process of concrete specimens. Before crack initiation, there are less AE events as there are very less microcracks in concrete, and the stress at crack tip is less. At the second stage, as load increases, cracks begins to form and increases steadily until the peak load. Therefore, the AE events increase steadily during the second stage. At postpeak, a large number of microcracks begin to aggregate into macrocrack. The growth rate of cumulative AE events is accelerating, and the AE signal is very active. In the fourth stage, as the macrocrack continues to expand, the crack tip gets closer to the bottom of the specimen. Influenced by the boundary effect, the local fracture energy of the specimen begins to decrease, and the growth rate of cumulative AE events begins to decrease. In addition, it can be seen that the cumulative AE events gradually decrease with the increase in the initial crack depth ratio of specimen, and this is consistent with the fracture energy. As the increase of the crack depth ratio results in the crack expansion space decreases. Influenced by the boundary effect, the critical crack length decreases gradually

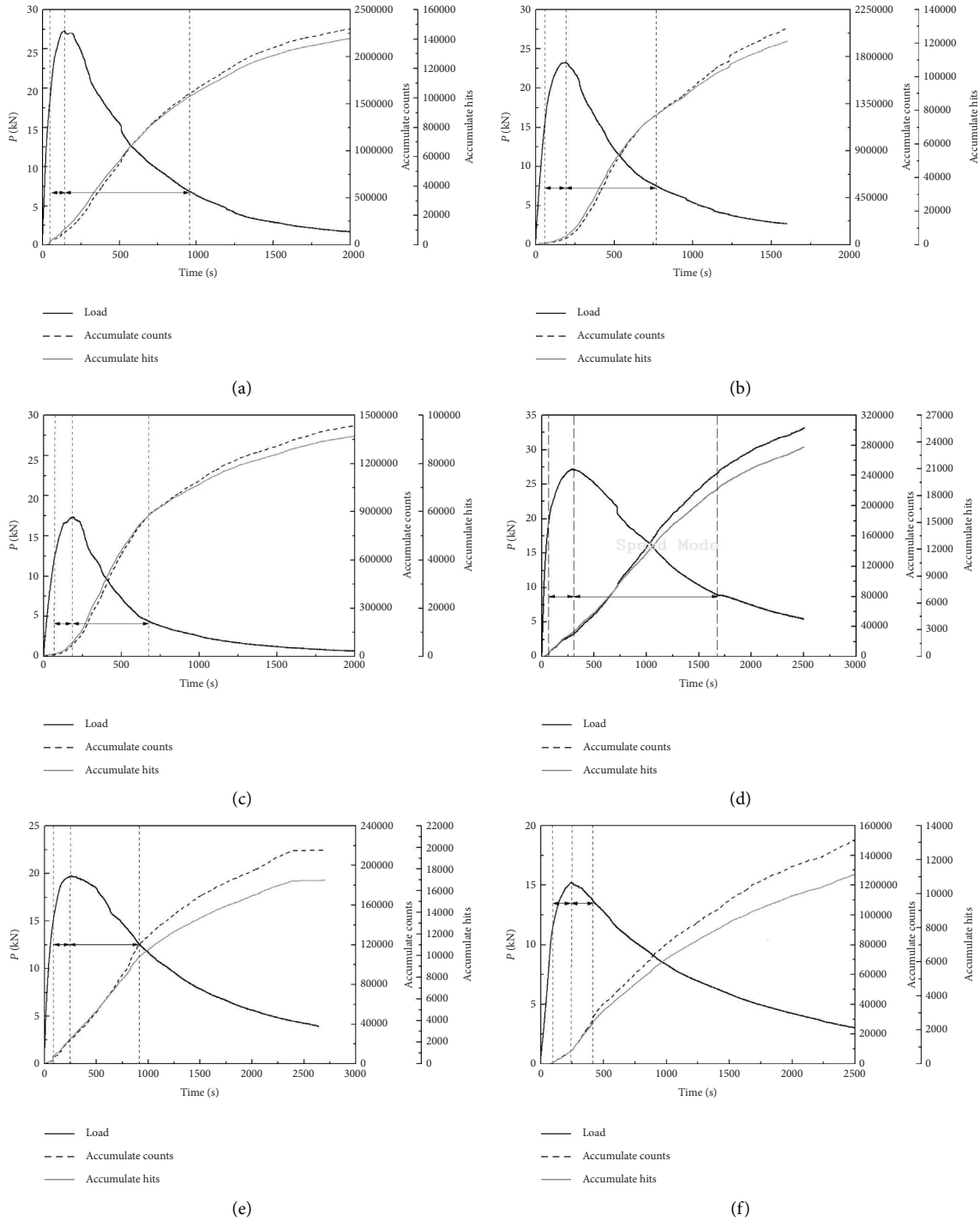

Figure 6: The cumulative AE counts and event time history curves. (a) WS300-0.3, (b) WS300-0.4, (c) WS300-0.5, (d) WS450-0.3, (e) WS450-0.4, and (f) WS450-0.5.

when it reaches the peak load. The four-stage characteristics of AE count and cumulative AE events can not only reflect the failure process of hydraulic concrete but also reflect the boundary effect on the fracture behavior of hydraulic concrete.

3.2.2. AE b Value. The *b* value can be used to measure the damage degree of concrete in the failure process [26]. In the AE monitoring technology, micro- or macrocracks produce AE signals of different amplitudes, and the microcracks with small amplitudes are more intense, while that with large

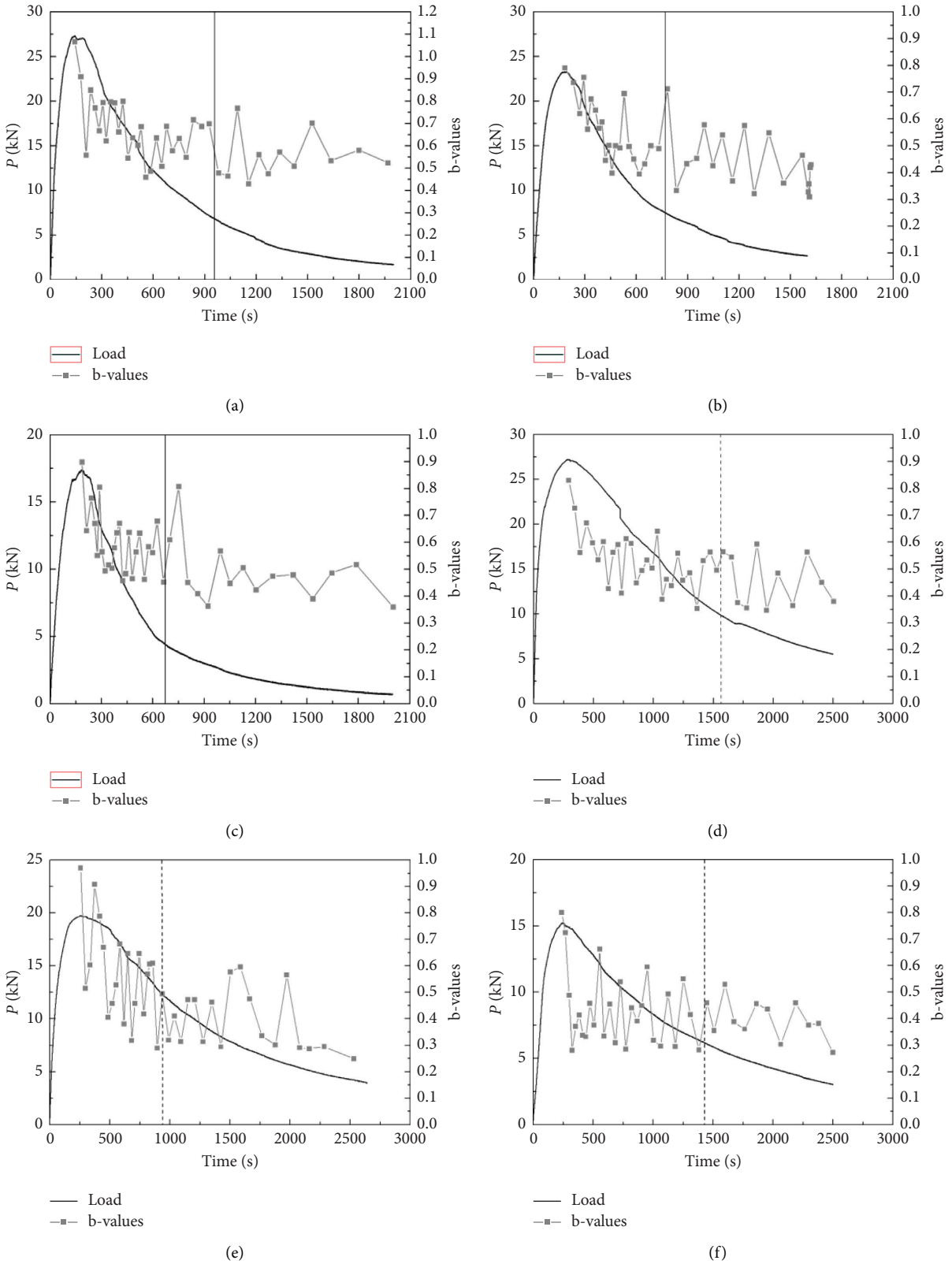

Figure 7: The AE *b* value of hydraulic concrete with different crack-depth ratios. (a) WS300-0.3, (b) WS300-0.4, (c) WS300-0.5, (d) WS450-0.3, (e) WS450-0.4, and (f) WS450-0.5.

amplitude is less. By calculating the AE-b value, the damage degree of concrete can be effectively evaluated. The g-R formula is modified as follows to calculate the AE b value [20]:

$$\log N = a - b\frac{A_{\mathrm{dB}}}{20}, \tag{5}$$

where N is the number of AE events whose amplitude is greater than A_{dB}, and A_{dB} is the peak amplitude of AE (dB).

Figure 7 shows the AE b values of hydraulic concrete with different crack-depth ratios. It can be seen that the AE b values fluctuate with time and generally show a downward trend, which can be divided into two stages. The AE b values are concentrated in the initial stage after peaking and tend to disperse later. The rising section of b value indicates the generation and aggregation of microcracks. When the microcracks accumulate to a certain number, they aggregate into macroscopic cracks, which can also be manifested by the decline of b value.

In the first stage, the b value decreases rapidly after the peak, indicating the rapid development of macrocracks. The b value fluctuates sharply and concentrates, indicating that acoustic emission activity is high and macrocracks are formed during the continuous generation, expansion, and aggregation of microcracks. In the second stage, the b value density is small, and the b value has a gentle downward trend, indicating that the macrocrack tends to be stable. The main crack has been formed, but the b value still fluctuates but it is relatively scattered, which indicates that the acoustic emission activity reduces, and the microcracks are aggregating into macrocrack. The variation trend of b value of hydraulic concrete specimens with different crack-depth ratios is similar. It can be seen from the load-time curve (Figure 7) that the postpeak load decline rate is fast at first and then slow. In the stage of rapid declination of postpeak load, AE b values are densely distributed and fluctuate violently. When the postpeak load declines slowly down, AE b values gradually become sparse. Compared with specimens with the side of 450 mm, the relationship between the postpeak AE b value and the declination rate of the postpeak load in specimens with the side of 300 mm is more obviously.

3.3. Crack Propagation Based on the DIC Method

3.3.1. Strain Field Analysis. For ease to study on strain field variation of the concrete specimen, the loading process is divided into 10 typical stages as shown in Figure 8. Figure 9 shows the strain field distribution cloud diagrams of WS300-0.3 obtained by the DIC method at different stages. It can be seen that at the initial stage, relatively scattered small strains are collected in the whole test area. This is the strain caused by the initial crack that forms during the moulding and curing process. At the peak load, the number of scattered strain concentration zone decreases gradually and converges at the crack tip, where the strain increases gradually, as shown in Figure 9(b). After reaching the peak load, the crack tip opening displacement (CTOD) exceeds the critical value CTOD_c. Therefore, the fictitious crack at the front of the initial crack tip gradually developed into the macroscopic crack. The microcrack near the crack tip increases and further aggregates. The secondary cracks disappear virtually, instead, the strain concentration area in the crack tip is obvious and the extension path is clear, as shown in Figure 9(c). As can be seen from Figure 9(d), the residual strain around the main crack is further released and the crack continues to spread forward along the main crack. Until it is loaded to the P_{10} stage, as shown in Figure 9(e), the strain in the area outside the main crack releases almost completely, and the strain is close to 0.

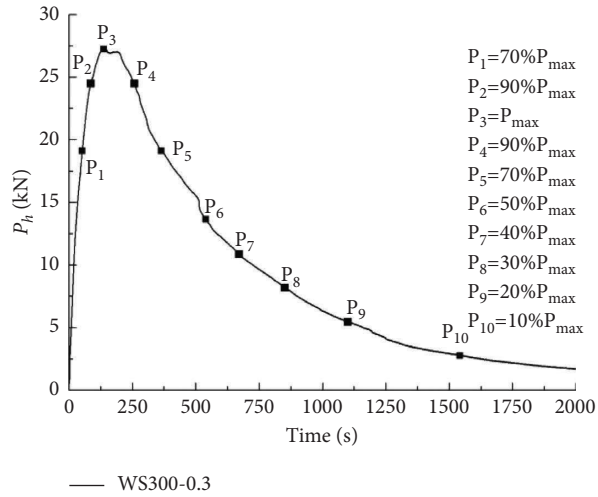

Figure 8: Typical loading stages of concrete during loading.

3.3.2. Crack Propagation. According to the displacement data obtained by the DIC method, the crack opening displacement (COD) along the main crack of the specimen can be calculated. According to the fictitious crack model, the effective crack of concrete includes macrocrack and fictitious crack, and the fictitious crack is the fracture process zone at front of crack tip. To be sure, the position of the crack tip is dynamically. When the CTOD at the crack tip exceeds the critical value CTODc, the crack tip also goes forward, that is, the fictitious crack expands to macrocrack, and the macrocrack increases, while the fictitious crack remains unchanged over a period of time. Figure 10 shows the variation of COD over the height of specimen WS300-0.3 at different loading stages. Coordinate Y represents the effective height of the specimen, and point O represents the position of the crack tip. The size of macrocrack, fictitious crack, and effective crack can be quantitatively determined according to the variation of COD. At P_1 stage, the CTOD is 0.022 mm, less than the critical value CTODc, so no macrocrack forms. At stage P_3, the CTOD reaches the critical value (0.068 mm), and the length of fictitious crack reaches 90.3 mm. As loading continues, the CTOD increases further and exceeds the critical value, macrocrack forms. When loading to stage P_5, COD and the length of effective crack increase obviously. The initial crack tip opening displacement reaches 0.21 mm, and the effective crack increases to 178.68 mm, covering macro crack 99.47 mm and fictitious crack 79.21 mm.

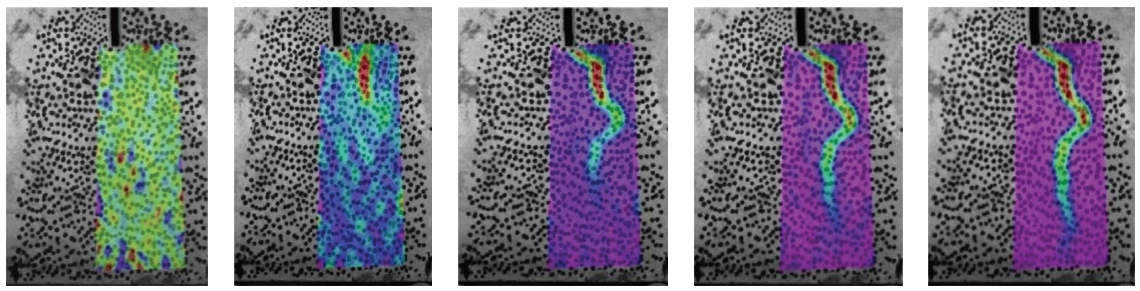

(a) (b) (c) (d) (e)

Figure 9: The strain field cloud picture at different loading stages. (a) P_1, (b) P_3, (c) P_5, (d) P_6, and (e) P_{10}.

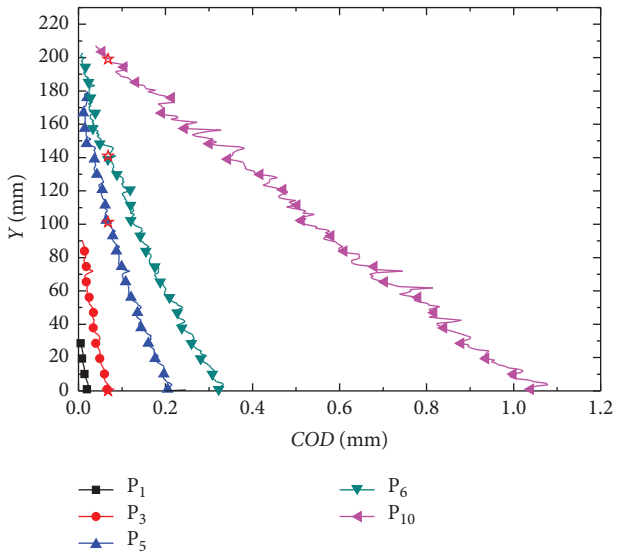

Figure 10: The variation of COD of specimen WS 300-0.3 at typical loading stages.

Meanwhile, a new crack tip formed, marked with an asterisk, as shown in Figure 10. At this stage, both the effective crack and macrocrack still grow rapidly, while the fictitious crack decreases gradually. When loading to stage P_6, the CTOD increases to 0.33 mm, and the effective crack length reaches 202.63 mm, covering the macrocrack 146.44 mm and the fictitious crack 56.19 mm. It shows that both the COD and effective crack increase slowly during this period, but the macrocrack dominates the effective crack. At stage P_{10}, the effective crack increases to 207.23 mm. The longitudinal crack development is restricted by the boundary during this stage. The macrocrack increases to 198.95 mm and the fictitious crack decreases to 8.28 mm. Meanwhile, the CTOD increases rapidly to 1.07 mm.

In order to further quantify the growth trend of crack at various loading stages and analyze the influence of crack-depth ratio on crack propagation, the evolution laws of macrocrack, fictitious crack, and effective crack are analyzed. Figure 11 shows the variation curves of macrocracks at various loading stages. It can be seen that, no macrocracks occur in the specimen before peak load. After loading to P_3 stage, the CTOD exceeds the critical value CTODc, and the macro crack forms rapidly, and the growth rate of the macrocrack length decreases with the increase of the initial crack depth ratio. This is because at the early stage, the number of microcracks in concrete increases with the decrease of the initial crack-depth ratio. When the CTOD exceeds the critical value, microcracks will quickly converge together and macro-cracks occur. The more the number of microcracks, the faster the macro-cracks develop. With continuous loading, the growth rate of macrocracks will be slowed down influenced by aggregate interlock and boundary constraint.

Figure 12 shows the change process of fictitious cracks in concrete specimens at various loading stages. The fictitious crack length increases at first and reaches the maximum value at P_3 stage, and the maximum fictitious crack decreases with the increase of the initial crack-depth ratio. This is because at initial loading stage, the COD at the crack tip does not reach the critical value, and the fictitious crack will gradually increase as load increases. When it exceeds the peak load, the CTOD reaches the critical value, and the development of the macro crack is faster than that of the effective crack, so the length of the fictitious crack will show a trend of rapid decline. Besides, the fictitious crack of WS300-0.4 shows a first increasing and then decreasing trend from stage P_5 to stage P_9. It can be found that in P_5 stage, crack propagation is affected by large aggregate, fictitious crack develops rapidly along the aggregate, and the macrocrack grows decreasingly rapidly. When the aggregate is fractured, the macrocrack develops rapidly again, and its expansion speed is much higher than that of the effective crack, and the fictitious crack decreases rapidly.

Figure 13 shows the variation of fictitious crack of concrete with three different crack-depth ratios at various loading stages. It can be seen from Figure 13, the development process of fictitious crack can be divided into three phases. The first stage includes loading stage P_0 to P_1 . In this period, due to the insufficient expansion of crack and interlocking between aggregate and crack, crack extension is prevented, growth of the effective crack is slow. In the second phase, from P_1 to P_5, as the biting pressure between aggregate and microcrack gradually decreases, the effective crack increases rapidly. P_5 to P_9 is the third phase. Influenced by the constraint of boundary and the increment of aggregate interlocking pressure, the growth of effective crack slows down. It can be seen from Figure 13 that at the first phase, the influence of the initial

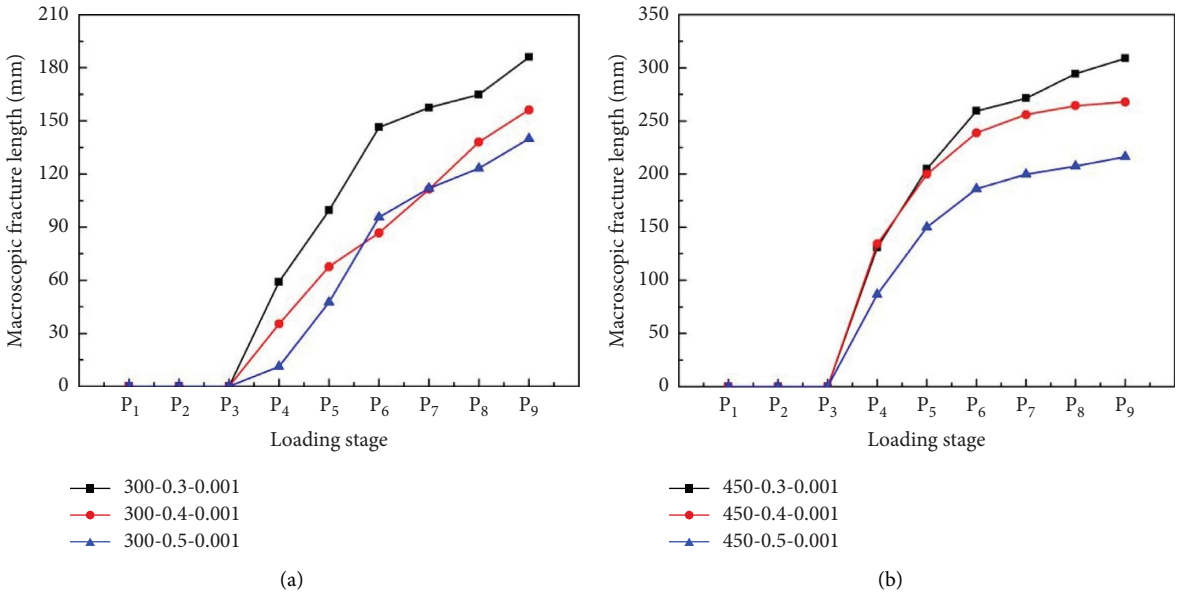

Figure 11: The variation of macrocrack with loading stage. (a) WS300. (b) WS450.

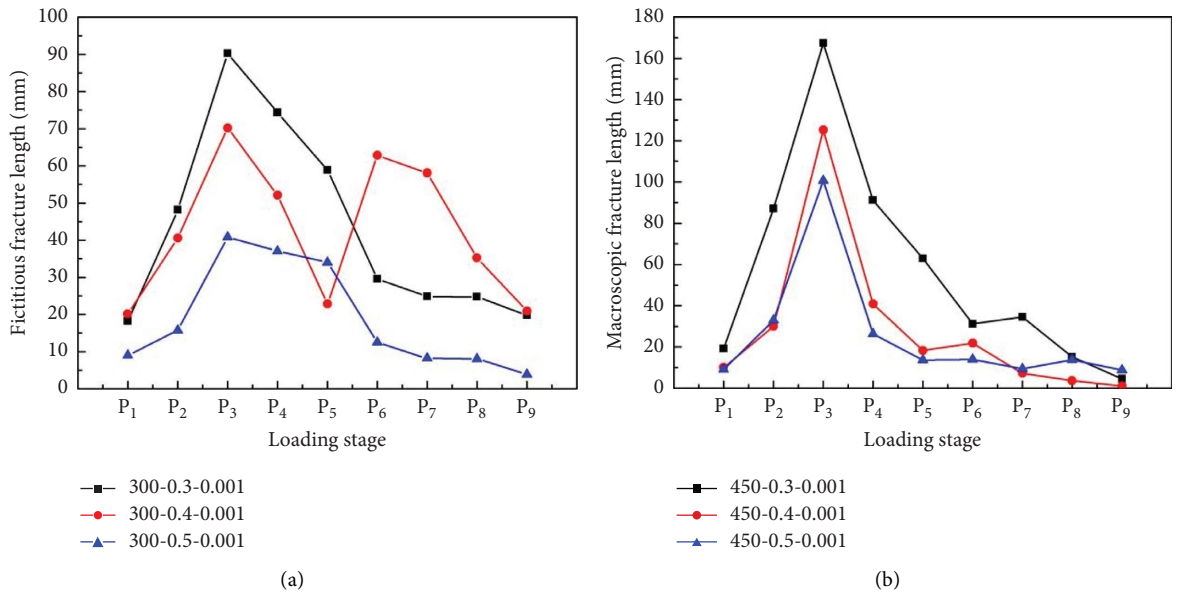

Figure 12: Variation of fictitious crack with loading stage. (a) WS300. (b) WS450.

crack-depth ratio on the effective crack is insignificant. This is because the biting pressure between cracks and aggregate inside concrete specimen, which is called the cohesion force. The crack was not fully developed at the initial loading stage, and the cracks was very short. The effect of the initial crack-depth ratio on the fracture development was not obvious. In the second phase, the effective crack length of concrete with smaller initial crack-depth ratio increases faster. This is because the smaller the initial crack depth ratio is, there is more space for crack to propagate inside the specimen, and more microcracks form. At stage P_1, microcracks near crack tip gradually converge to macro-cracks at a faster rate. The larger the initial crack-depth ratio is, the more obvious the effect of boundary is, the less microcracks formed, and the slower the formation and development of main cracks are. In the third phase, the effective crack length of specimen WS300-0.5 increases by 46.7 mm, which is much larger than 30.62 mm of specimen WS300-0.3. However, the effective crack length of specimen WS450-0.5 increased by 61.5 mm, which was also much larger than 45.84 mm of specimen WS300-0.3. This indicates that the effective crack length increases more obviously in the third stage with the increase of the initial crack-depth ratio.

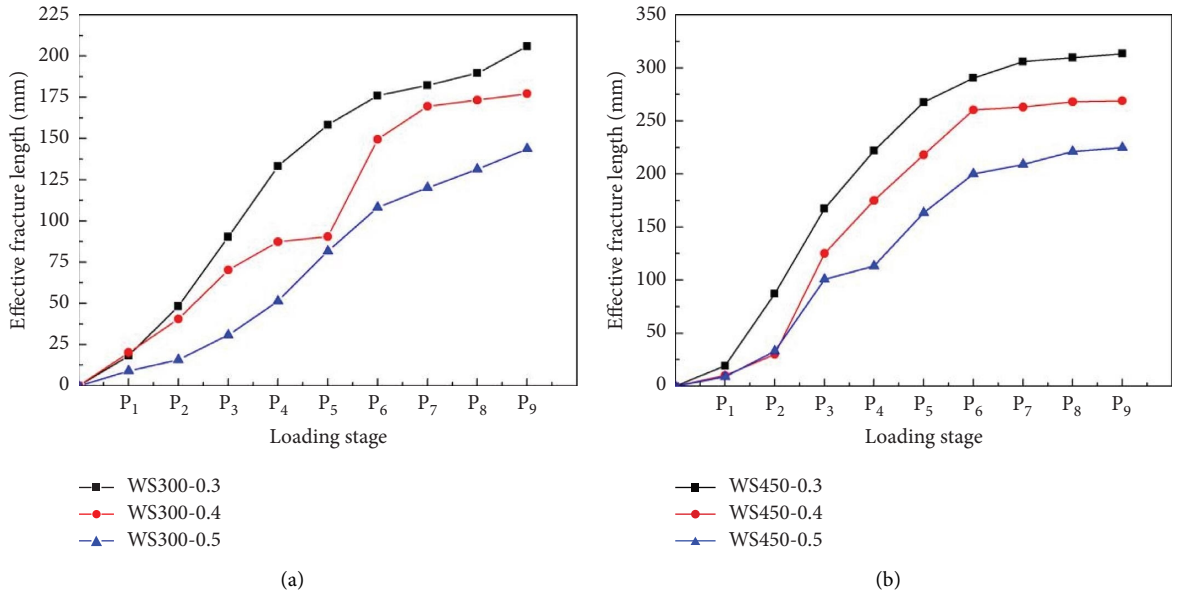

Figure 13: The variation of the effective crack length with loading stage. (a) WS300. (b) WS450.

Table 3: The effective crack length Δa_{fic} and β.

Specimen	a_0 (mm)	α_0	W-a_0 (mm)	d_{max} (mm)	Δa_{fic} (mm)	β
WS300-0.3	90	0.3	210	80	90.26	1.13
WS300-0.4	120	0.4	180	80	70.23	0.88
WS300-0.5	150	0.5	150	80	40.83	0.51
WS450-0.3	135	0.3	315	120	167.45	1.40
WS450-0.4	180	0.4	270	120	125.21	1.04
WS450-0.5	225	0.5	225	120	100.73	0.84

3.3.3. Relationship between Effective Crack and Maximum Aggregate Size. In this paper, it is found that maximum aggregate size and specimen size have important effects on crack propagation. The relationship between effective crack length Δa_{fic} and maximum aggregate size d_{max} can be expressed by the following formula:

$$\Delta a_{fic} = \beta \cdot d_{max}, \tag{6}$$

in which β is an empirical parameter, called aggregate coefficient.

Table 3 shows the calculation results of effective crack length Δa_{fic} and β under peak load. It can be seen that the β value of specimens with side length of 300 mm ranges from 0.51 to 1.13, and the average effective crack length Δa_{fic} is 0.88 times the maximum aggregate size d_{max} (80 mm). The β value of specimens with side length of 450 mm ranges from 0.84 to 1.4 mm, and the average effective crack length Δa_{fic} is 1.1 times of the maximum aggregate size d_{max} (120 mm). For specimens with the same side length, it can be found that the β increases with the decrease of the initial crack-depth ratio. In the case of the same initial crack-depth ratio, β increases with the increase of specimen side length, which indicates that when a_0/W is smaller or W is larger, there is more space for longer effective crack in specimen. This is consistent with the variation rule of β values measured by Hoover and Bazant [2] on specimens with different sizes. The effective crack length Δa_{fic} and β decrease with the increase of the initial crack-depth ratio when the specimen size remains unchanged. It indicates that the maximum aggregate size has an effect on the parameter β, which is consistent with the conclusion that coarse and highly heterogeneous of aggregate has effect on the crack propagation of concrete expressed by formula (6). It indicates that the crack propagation is not only affected by boundary, but also by the maximum aggregate size.

4. Conclusions

(1) Influenced by the boundary effect, with the increase of crack depth ratio, the peak load, unstable fracture toughness, fracture energy, and critical crack length of hydraulic concrete gradually decrease. The initial fracture toughness is basically unchanged. When the initial crack-depth ratio is same, the toughness of concrete increases with the increasing of specimen size.

(2) Cumulative AE count and AE events curves can reflect the four-stage fracture characteristics and the boundary effect of hydraulic concrete. AE b value can well reflect the fracture mode of concrete at postpeak stage.

(3) The smaller the initial crack-depth ratio is, crack propagates more fully. So the whole fictitious crack and the effective crack increase as the initial crack-depth ratio decreases. At the same time, the

macrocrack growth rate is faster when the initial crack-depth is smaller.

(4) The crack propagation is not only influenced by the side length and the initial crack-depth ratio but also influenced by the maximum aggregate size. The larger the maximum aggregate size is, the larger the effective crack length is, and the effective crack length increases with the increase of the effective height of the specimen and aggregate particle size.

Data Availability

The data that support the findings of this study are available from the corresponding author.

Conflicts of Interest

The authors declare that there are no conflicts of interest.

Acknowledgments

The Open Foundation of State Key Laboratory of Hydrology-Water Resources and Hydraulic Engineering (Grant no. 2017491711).

References

[1] M. F. Kaplan, "Crack propagation and the fracture of concrete," *ACI Materials Journal*, vol. 58, no. 11, pp. 591–610, 1961.

[2] C. G. Hoover and Z. P. Bazant, "Universal size-shape effect law based on comprehensive concrete fracture tests," *Journal of Engineering Mechanics*, vol. 140, no. 3, pp. 473–479, 2014.

[3] T. Tang, Z. P. Bazant, S. Yang, and D. Zollinger, "Variable-notch one-size test method for fracture energy and process zone length," *Engineering Fracture Mechanics*, vol. 55, no. 3, pp. 383–404, 1996.

[4] Y. B. Ma, Y. Qin, J. R. Chai, and X. Zhang, "Analysis of the effect of initial crack length on concrete members using extended finite element method," *International Journal of Civil Engineering*, vol. 17, no. 10, pp. 1503–1512, 2019.

[5] J. D. Liu, X. Fan, and C. Y. Shi, "Effect of initial crack-depth ratio on fracture characteristics of FRP-strengthened concrete," *Fatigue and Fracture of Engineering Materials and Structures*, vol. 44, no. 7, pp. 1708–1718, 2021.

[6] P. Xu, J. Y. Ma, M. X. Zhang, Y. Ding, and L. Meng, "Fracture energy analysis of concrete considering the boundary effect of single-edge notched beams effect of single-edge notched beams," *Advances in Civil Engineering*, vol. 2018, Article ID 3067236, 10 pages, 2018.

[7] S. W. Hu, J. F. Xie, and Q. Y. Chen, "XDEM simulation and analysis of wedge splitting fracture process of concrete," *Water Resources and Power*, vol. 34, no. 5, pp. 120–123, 2016.

[8] Y. Q. Hu, S. W. Hu, and Y. Q. Huang, "Experimental studies on mechanical properties and Kaiser effect of concrete with cracks under axial tensile stress," *Hydro-Science and Engineering*, vol. 3, pp. 67–75, 2019.

[9] W. L. Xu, B. Chen, X. D. Chen, and C. Chen, "Influence of aggregate size and notch depth ratio on fracture performance of steel slag pervious concrete," *Construction and Building Materials*, vol. 273, Article ID 122036, 2021.

[10] X. Z. Hu, J. F. Guan, Y. S. Wang, A. Keating, and S. Yang, "Comparison of boundary and size effect models based on new developments," *Engineering Fracture Mechanics*, vol. 175, pp. 146–167, 2017.

[11] Y. S. Wang, X. Z. Hu, L. Liang, and W. Zhu, "Determination of tensile strength and fracture toughness of concrete using notched 3-p-b specimens," *Engineering Fracture Mechanics*, vol. 160, pp. 67–77, 2016.

[12] J. F. Guan, X. Z. Hu, C. P. Xie, Q. Li, and Z. Wu, "Wedge-splitting tests for tensile strength and fracture toughness of concrete," *Theoretical and Applied Fracture Mechanics*, vol. 93, pp. 263–275, 2018.

[13] R. J. Li, Z. G. Zhu, X. H. Yao, and X. Y. Zhang, "Study on effect of different fine aggregates on properties of dam concrete," *Applied Mechanics and Materials*, vol. 439, pp. 174–178, 2013.

[14] G. X. Chen and F. T. Jiang, "Analysis of the factors affecting crack resistance of dam concrete," *Key Engineering Materials*, vol. 533, pp. 302-303, 2005.

[15] N. W. Xu, F. Dai, C. Sha, Y. Lei, and B. Li, "Microseismic signal characterization and numerical simulation of concrete beam subjected to three-point bending fracture of concrete beam subjected to three-point bending fracture," *Journal of Sensors*, vol. 2015, Article ID 987232, 11 pages, 2015.

[16] M. Rady, S. Y. Mahfouz, and F. Yousse, "Effects of concrete grades and column spacings on the optimal design of reinforced concrete buildings," *Materials*, vol. 15, no. 12, p. 4290, 2022.

[17] S. Hatanaka, N. Mishima, A. Maegawa, and E. Sakamoto, "Fundamental study on properties of small particle size porous concrete," *Journal of Advanced Concrete Technology*, vol. 12, no. 1, pp. 24–33, 2014.

[18] Y. Shi, X. D. Lv, S. H. Zhou et al., "Mechanical properties, durability, and ITZ characteristics of full-grade dam concrete prepared by aggregates with surface rust stains," *Construction and Building Materials*, vol. 305, Article ID 124798, 2021.

[19] A. Panjsetooni, N. M. Bunnori, A. H. Vakili, Z. Shirkhani, and Z. Shirkhani, "Fracture Formation evaluation of reinforced concrete structure using acoustic emission technique," *Chinese Journal of Engineering*, vol. 2013, Article ID 126509, 7 pages, 2013.

[20] C. Chen, X. Q. Fan, and X. D. Chen, "Experimental investigation of concrete fracture behavior with different loading rates based on acoustic emission," *Construction and Building Materials*, vol. 237, Article ID 117472, 2020.

[21] A. A. Abouhussien and A. A. A. Hassan, "Classification of damage in self-consolidating rubberized concrete using acoustic emission intensity analysis," *Ultrasonics*, vol. 100, Article ID 105999, 2020.

[22] S. H. Dai, X. L. Liu, and K. Nawnit, "Experimental study on the fracture process zone characteristics in concrete utilizing DIC and AE methods," *Applied Sciences*, vol. 9, no. 7, p. 1346, 2019.

[23] E. B. Pereira, G. Fischer, and J. A. Barros, "Direct assessment of tensile stress-crack opening behavior of strain hardening cementitious composites (SHCC)," *Cement and Concrete Research*, vol. 42, no. 6, pp. 834–846, 2012.

[24] DL/T5332-2005, *Norm for Fracture Test of Hydraulic Concrete*, China Electric Power Press, Bei jing, China, 2006.

[25] J. P. Ulfkjær, S. Krenk, and R. Brincker, "Analytical model for fictitious crack propagation in concrete beams," *Journal of Engineering Mechanics*, vol. 121, no. 1, pp. 7–15, 1995.

[26] Y. Z. Guo, X. D. Chen, H. Q. Yang, L. Hu, J. Zhang, and X. Fan, "Experimental study on direct tension behavior of concrete through combined digital image correlation and acoustic emission techniques," *Structural Concrete*, vol. 20, no. 6, pp. 2042–2055, 2019.